RSC Advances

PAPER

View Article Online
View Journal | View Issue

Cite this: *RSC Adv.*, 2019, **9**, 42316

MoS_2/carbon composites prepared by ball-milling and pyrolysis for the high-rate and stable anode of lithium ion capacitors†

Chong Wang,[a] Changzhen Zhan,[a] Xiaolong Ren,[a] Ruitao Lv,[a] Wanci Shen,[a] Feiyu Kang[bc] and Zheng-Hong Huang *[ab]

Lithium ion capacitors (LICs), bridging the advantages of batteries and electrochemical capacitors, are regarded as one of the most promising energy storage devices. Nevertheless, it is always limited by the anodes that accompany with low capacity and poor rate performance. Here, we develop a versatile and scalable method including ball-milling and pyrolysis to synthesize exfoliated MoS_2 supported by N-doped carbon matrix derived from chitosan, which is encapsulated by pitch-derived carbon shells (MoS_2/CP). Because the carbon matrix with high nitrogen content can improve the electron conductivity, the robust carbon shells can suppress the volume expansion during cycles, and the sufficient exfoliation of lamellar MoS_2 can reduce the ions transfer paths, the MoS_2/CP electrode delivers high specific capacity (530 mA h g^{-1} at 100 mA g^{-1}), remarkable rate capability (230 mA h g^{-1} at 10 A g^{-1}) and superior cycle performance (73% retention after 250 cycles). Thereby, the LICs, composed of MoS_2/CP as the anode and commercial activated carbon (21 KS) as the cathode, exhibit high power density of 35.81 kW kg^{-1} at 19.86 W h kg^{-1} and high energy density of 87.74 W h kg^{-1} at 0.253 kW kg^{-1}.

Received 12th November 2019
Accepted 12th December 2019

DOI: 10.1039/c9ra09411c

rsc.li/rsc-advances

Introduction

With the increasingly serious environmental concerns and the shortage of clean and sustainable resources, there are an increasing number of scientific research works concentrating on constructing superior energy storage devices.[1–4] Over the years, lithium ion batteries and supercapacitors have been two dominant energy storage devices, which attract unprecedented attentions. Because LIBs and ECs store energy by faradaic reactions and electrostatic charge adsorption respectively, LIBs deliver high energy density (>180 W h kg^{-1}) but unoptimistic power density (<1000 W kg^{-1}) with short cycle period (<500 cycles), and ECs exhibit excellent power density (>10 000 W kg^{-1}) and remarkable cycle stability (>10 000 cycles) but inferior energy density (<10 W h kg^{-1}).[5–8] Therefore, lithium ion capacitors (LICs), which can bridge the merits of LIBs and ECs, is promising to be new generation of advanced energy storage devices in the future.[9–11]

There are two basic types of lithium ion capacitors (LICs). One is the configuration of battery-type cathode and capacitor-type anode, such as (−) AC//$LiMn_2O_4$ (+).[12] The kind of LICs has narrow voltage windows because the stable potential range of AC is 1.5–4.5 V. Therefore, it has low energy density. As for power density, the battery-type cathode cannot satisfy the rate demand so that the introduction of conductive materials is necessary. However, the measure would decrease the capacity of cathode and the energy of LICs. The other is the construction of capacitive cathode and battery-type anode.[9,13–16] In 2001, Amatucci *et al.* had developed the system which consists of nano-$Li_4Ti_5O_{12}$ as the battery-type anode and N-doped activated carbon as the capacitor-type cathode.[17] However, on account of the different mechanisms of energy storage, the power and energy densities depends on the faradaic-type anode with sluggish reaction kinetics and the adsorption-type cathode with low capacity, respectively.[18,19] It is an urgent and everlasting goal to construct an anode with high rate performance and long cycle life so that the whole device can deliver better performance by remedying the mismatch of kinetics and capacity between the cathode and anode.

MoS_2 (molybdenum disulfide), as one of the family of bidimensional layered metal sulfides, has attracted many researchers' attention.[20–22] It possesses large interlayers distance (0.615 nm) and well-defined 2D plane structure. MoS_2

[a]*State Key Laboratory of New Ceramics and Fine Processing, School of Materials Science and Engineering, Tsinghua University, Beijing 100084, P. R. China. E-mail: zhhuang@tsinghua.edu.cn*

[b]*Key Laboratory of Advanced Materials (MOE), School of Materials Science and Engineering, Tsinghua University, Beijing 100084, China*

[c]*Engineering Laboratory for Functionalized Carbon Materials, Graduate School at Shenzhen, Tsinghua University, Shenzhen 518055, P. R. China*

† Electronic supplementary information (ESI) available: SEM spectra of chitosan, cg-MoS_2 and MoS_2/C. XPS data of N-doped carbon matrix and MoS_2/C. Raman images, GCD curves and CV curves of bulk MoS_2 and MoS_2/C. N_2 adsorption/desorption isotherms, pore size distribution (PSD), CV and GCD curves of 21 KS. Element atom ratio of three samples. See DOI: 10.1039/c9ra09411c

demonstrates low reaction potential and high theoretical capacity of 669 mA h g^{-1} as promising anode materials.[23] Nonetheless, the electrochemical performance of MoS_2 is subject to its terrible intrinsic conductivity and severe volume changes during cycles, which will bring about the pulverization of electrode and the failure of active materials.[24–26] Recently, there are some strategies, such as preparing nano-sized MoS_2,[27,28] mixed with conductive carbon matrix,[29–31] and increasing the interlayer distance,[22,32] to compensate the above shortage. However, many above synthetic methods are complicated and difficult for scale production so that researchers are looking forward to finding simple and scalable ways to synthesizing MoS_2-based anode materials with superior rate property and long cycle life. Sun *et al.*[33] obtain MoS_2/graphene nanosheets from bulk MoS_2 and commercial graphite through two-step ball-milling method and the materials deliver outstanding electrochemical properties. According to our survey findings, there are few reports about exfoliating and then coating MoS_2 by other carbon sources in the up-down methods so far.

Here, we used a ball-milling approach to prepare chitosan-grafted MoS_2 with few layers (cg-MoS_2) from chitosan and commercial bulk MoS_2. Then we successfully synthesized the exfoliated MoS_2 supported by N-doped carbon matrix derived from chitosan, which is encapsulated by pitch-derived carbon shells (MoS_2/CP) through one-step heat treatment of the cg-MoS_2 mixed with the pitch (Scheme 1). Because the few-layered MoS_2 is uniformly distributed in the conductive carbon matrix with high nitrogen content, it possesses superior electron conductivity and short ion/electron transfer paths. What's more, the pitch melts and flows onto the surface of the cg-MoS_2 particles at about 270 °C during pyrolysis process so that a close contact is formed between the MoS_2 nanosheets and the robust carbon shells, which can restrain the volume expansion and pulverization. For LIBs, MoS_2/CP exhibits high capacity (530 mA h g^{-1} at 100 mA g^{-1}), ultrahigh rate capability (230 mA h g^{-1} at 10 A g^{-1}) and stable cycle (73% capacity retention after 250 cycles). When matched with commercial AC (21 KS) as cathode, the fabricated LICs deliver high energy density of 87.74 W h kg^{-1} at 0.253 kW kg^{-1}, superb power density of 35.81 kW kg^{-1} even at 19.86 W h kg^{-1} and superior cycling durability (79.61% capacity retention after 1000 cycles). Consequently, we demonstrate the composites synthesized by the versatile methods show superb electrochemical property and have certain application prospects in LIBs and LICs.

Experimental

Preparation of N-doped carbon matrix, MoS_2/C and MoS_2/CP

In a typical ball-milling process, 5 g commercial bulk MoS_2 (Aladdin, 99.5%, <2 μm), 10 g chitosan (Biochemical Reagent) and four sorts of ZrO_2 balls with diameters of 2 mm (100 g), 4 mm (60 g), 6 mm (20 g) and 10 mm (20 g) were mixed into a ZrO_2 tank (volume = 140 mL). The weight ratio of ball to sample was between 15 : 1 to 10 : 1 and each of them accounted for 1/3 of the tank volume. Then the tank operated at a rotational rate of 450 rpm for 12 h in a planetary ball-milling machine (MITR-YXQM-0.4L) to produce cg-MoS_2. Then 1.5 g petroleum pitch powder was mixed with 15 g cg-MoS_2 in the tank and they were rotated at a speed of 300 rpm for 1 hour to

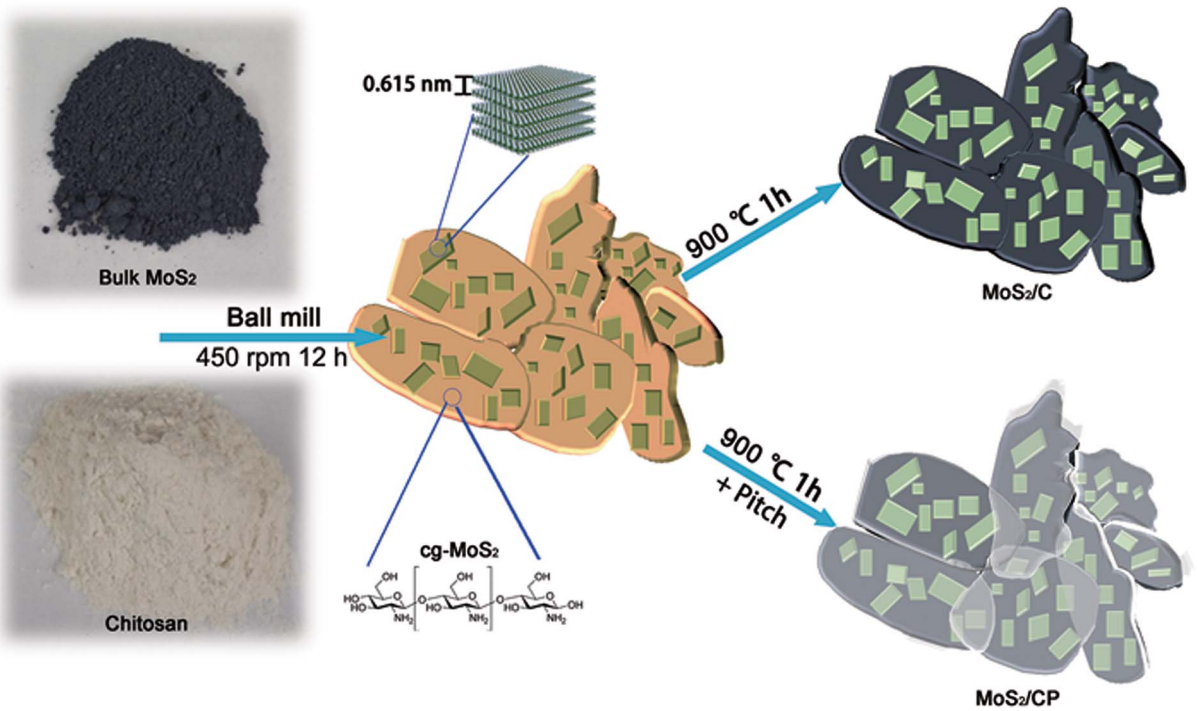

Scheme 1 Illustration of the ball-milling and pyrolysis process.

get homogeneous mixture. After the mixture was heated at 900 °C for 1 hour at a ramp rate of 2 °C min^{-1}, we got the products-MoS_2/CP. The contrast sample-MoS_2/C was synthesized in the same way without pitch. The N-doped carbon matrix was synthesized with the chitosan through the same heat treatment.

Characterization

The scanning electron microscopy (LEO 1530), transmission electron microscopy (Tecnai G20) and X-ray diffraction (Bruker D8) were employed to characterize the morphology and structure of the samples. The valence states and element types on the sample surface were analyzed by X-ray photoelectron spectroscopy (PHI Quantera Imaging). Raman scattering (Renishaw, In Via-Reflex, $\lambda = 532$ nm) was mainly used to reveal the structural features of MoS_2 and carbon. The content of each constituent was measured by Thermo-gravimetric Analysis (Mettler Toledo) in air at a ramp rate of 5 °C min^{-1} from 25 °C to 700 °C. The Brunauer–Emmett–Teller method and density functional theory (DFT) were utilized to calculate the specific surface areas and pore size distribution through the N_2 sorption/desorption isotherms. The DFT describes the distribution characteristics of adsorbed molecules in the pore, which is based on the statistic mechanics. We can obtain reliable pore size analysis in the whole pore range (including micropore and mesoporous) in the DFT-based method.

Fabrication of the cells

Active materials (80%), super P (10%) and poly (vinylidene fluoride) (10%) were mixed in excess NMP solvent to form a homogenous slurry. Then it was spread on the Cu foil for the anode and on the Al foil for the cathode. The foils were dried for 24 h in vacuum oven at 120 °C and then punched into discs for cell fabrication. The mass loading density of cathode was controlled from 1.7 mg cm^{-2} to 2.8 mg cm^{-2} and that of anode was fixed at about 1.1 mg cm^{-2}. Half-cells were assembled in coin cell CR-2032 while the counter electrode was the Li metal sheet and the electrolyte was 1 M $LiPF_6$ in EC/DEC (vol% = 1 : 1). For LICs, the anode was discharged to the cut-off potential 0.7 V after 3 cycles at 0.1 A g^{-1} and then assembled with cathode of different mass for the capacity balance.

Electrochemical measurements

The galvanostatic charge/discharge (GCD) test of half cells was operated by a LAND battery system (Jinnuo Electronics Co.) and the voltage window was set in 0.01–3.0 V *vs.* Li/Li^+. The Arbin-BT 2000 test equipment and VSP-300 electrochemical analyzer were used to accomplish the GCD and cyclic voltammetry (CV) tests of LICs in the voltage windows of 1.0–4.0 V. Electrochemical impedance spectroscopy (EIS) test was performed in the frequency area of 1 M Hz to 10 m Hz with an AC amplitude of 10 mV.

Results and discussion

The chitosan is chosen as the carbon precursor due to its high carbon and nitrogen content. Moreover, many –OHs also facilitate the peeling of bulk MoS_2 through the bonding between oxygen atom and Mo atom and preventing exfoliated MoS_2 to stack with each other.[34] As shown in Fig. 1a, the bulk MoS_2 is clastic with a length of 1–2 μm. The SEM image (Fig. S1†) of chitosan presents a dense nubby structure with a diameter of

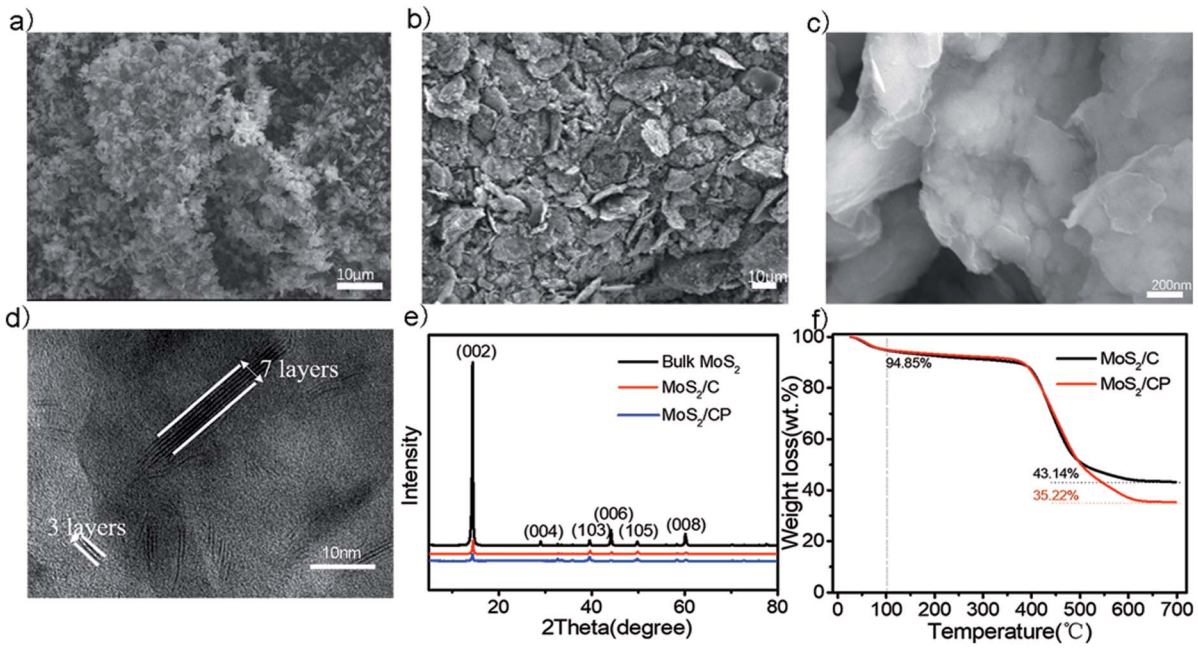

Fig. 1 Morphological, structural and component characterization of samples. (a) SEM images of bulk MoS_2, (b and c) SEM images of MoS_2/CP, (d) TEM image of MoS_2/CP, (e) XRD patterns of bulk MoS_2, MoS_2/C and MoS_2/CP, (f) TGA of MoS_2/C and MoS_2/CP.

10–30 μm. The cg-MoS_2 (Fig. S2†) has smaller particle sizes and the MoS_2 sheets are attached uniformly on the chitosan after ball-milling process. The pitch can melt at about 270 °C and flow onto the surface of cg-MoS_2 to form compact shells after carbonization.[35,36] Therefore the MoS_2/CP particles present a lenticular shape on the whole and a layer of hazy membrane on its surface in Fig. 1b and c. MoS_2/C is carbonized from cg-MoS_2 without pitch and presents bare MoS_2 nanosheets on the carbon matrix (Fig. S3†).

The X-ray diffraction (XRD) results (Fig. 1e) shows that the crystal lattice of as-prepared MoS_2/CP and MoS_2/C are in accord with that of 2H-MoS_2 (JCPDS PDF#37-1492) and the peak intensity of (002) crystal plane presents prominent recede while that of other-directional crystal planes becomes more obvious.[27,37,38] As shown in Fig. 1d, the transmission electron microscopy images explain that the exfoliated MoS_2 is mostly 3–7 layers and the interlayer spacing of 0.62 nm corresponds to the (002) crystal face of 2H-MoS_2.[39] It also demonstrates the exfoliation of bulk MoS_2 is fairly sufficient, which is consistent with the XRD results. The Raman spectra (Fig. S4†) has obvious characteristics of MoS_2, namely peaks at 403 cm^{-1} and 375 cm^{-1} reflect the A_{1g} and E^1_{2g} vibration modes of Mo–S bond, respectively.[40] The G band at 1581 cm^{-1} shows relatively intense in comparison to the D band at 1345 cm^{-1}, which suggests that the dominant form of carbon in the samples is disordered carbon.[41] TGA curves are showed in the Fig. 1f. It must also be mentioned that the final residue is MoO_3 converted from MoS_2 and other components are oxidized to gases. According to this reaction process, we calculate the mass ratio of MoS_2 in MoS_2/C and MoS_2/CP is 50.56% and 41.44%, respectively.[26,32]

According to the X-ray photoelectron spectroscopy shown in Fig. 2a–d, the surface chemical states of MoS_2/CP are examined. The peaks at about 284.8 eV, 285.7 eV, 286.9 eV and 289.7 eV can be separated from the C 1s region, which are assigned to the C–C, C–N, C–O and O–C=O species.[42,43] The peak at 398.3 eV in the N 1s spectrum corresponds to the pyridinic N, which is the main form of nitrogen in the sample while the peaks at 400.7 eV is deemed to the graphitic N.[27,42] Due to the kinetics-controlled lithium storage process, the introduction of heteroatoms can cause some vacancies and/or redundant electrons so that the conductivity may be improved.[44] As for nitrogen element, the pyridinic N can also provide more capacity.[45] The intense peak at 395.4 eV is attributed to the Mo $3p_{3/2}$.[46] We can see from Fig. 3c that Mo element have two oxidation states. Mo^{4+} at the edge of MoS_2 sheets is easier to be oxidized to Mo^{6+} during ball-milling and pyrolysis process.[25,27] The XPS curves of N-doped carbon matrix and MoS_2/C are shown in Fig. S5 and S6.† The atom ratio of three samples is shown in Table S1.† It is calculated from the integral peak areas. The Mo : S atom ratio is about 2.02, which is consistent with the raw material-MoS_2. Notably, the carbon to oxygen ratio of carbon matrix is clearly higher than that of MoS_2/C and MoS_2/CP. Thus the oxygen atoms in the chitosan are really combined with the Mo atoms at the edge zone so that the confined oxygen atoms would remain in the sample during the heat treatment according to the previous literature.[33] The nitrogen atom ratio of MoS_2/C and MoS_2/CP is about 6.1%, which is beneficial to the electrochemical property.

According to the CV curves tested at 0.2 mV s^{-1} in Fig. 3a, the electrode reactions are investigated. In the 1st cathodic sweep,

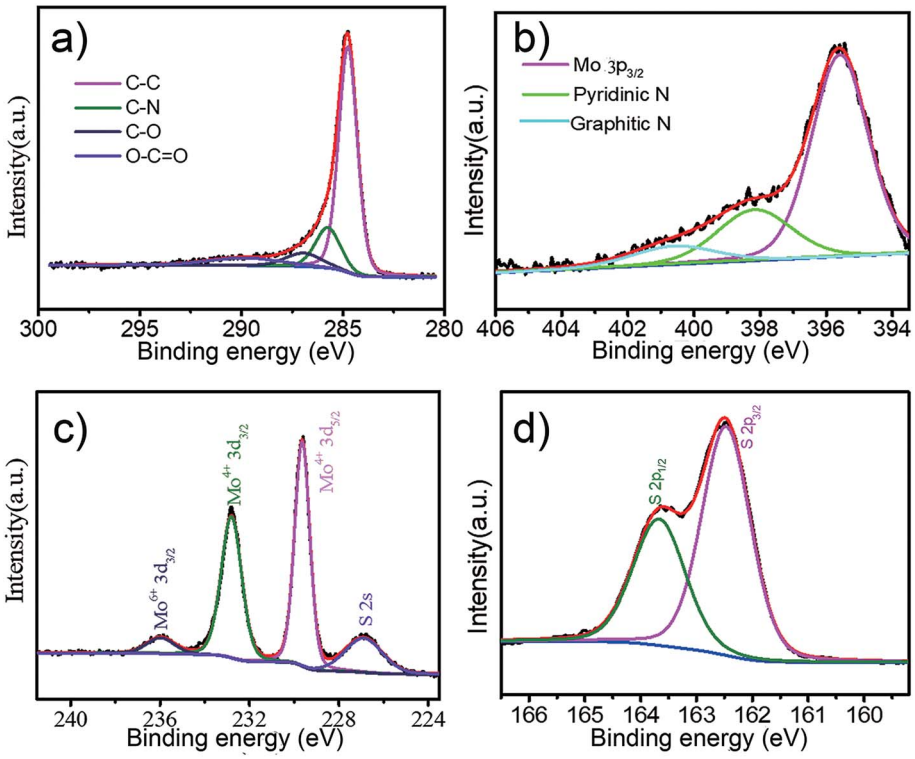

Fig. 2 XPS results of MoS_2/CP: C 1s (a), N 1s (b), Mo 3d (c) and S 2p (d).

the broad peak at about 0.85 V corresponds to the formation of Li_xMoS_2 with octahedral structure due to the insertion of Li^+ into MoS_2 interlayers, and the peak at about 0.3 V is attributed to the conversion reaction from Li_xMoS_2 to Mo atom and the formation of solid electrolyte interphase resulted from the decomposition reaction of electrolyte.[47] In the 2nd and 3rd cathodic sweeps, two new peaks at 1.8 V and 1.0 V may arise from the multistep Li^+ insertion mechanism as follows:[47,48]

$$2Li^+ + 2\,e^- + S \rightarrow Li_2S \quad (1)$$

$$MoS_2 + xLi^+ + xe^- \rightarrow Li_xMoS_2 \quad (2)$$

And the broad peak or shoulder at about 0.3 V is attributed to the complete transformation reaction from Li_xMoS_2 to Mo atom and Li_2S.[47] As for anodic sweeps, the former poor peak at 1.7 V is mainly ascribed to the partial transformation from Mo atom to MoS_2, while the latter obvious peak at about 2.3 V indicates the oxidation of Li_2S to sulfur.[47,49] Since the 3rd cycle, the shape of CV curves has little change, which suggests the SEI has become stable. Identical conclusions can be learned from the first three laps of charge/discharge profiles in Fig. 3b. MoS_2/CP exhibits high reversible capacity (520 mA h g^{-1} at 100 mA g^{-1}) and has slightly higher initial Coulombic efficiency (ICE) of 73.15% compared with MoS_2/C (Fig. S7a†). The ICE of the bulk MoS_2 is 79.48% (Fig. S8a†) and it is higher than that of MoS_2/CP and MoS_2/C owing to the more exposed zone of exfoliated MoS_2 and the introduction of carbon.

The kinetics analysis of three samples is carried out by the CV curves at diverse scan rates, aiming to comprehend the electrochemistry behaviours. A valid method has been reported previously to analyse the Li^+ storage kinetics.[50] There is a relationship between peak current density (i) and scan rates (v) as follows:

$$i = av^b \quad (3)$$

where the parameters a and b are constants. The b value can be calculated by the method of linear fitting. If $b = 0.5$, it is on behalf of complete battery behaviour with diffusion-controlled electrode reaction. If $b = 1$, it represents capacitive behaviour.[51] The b values of many materials are between 0.5 and 1. The b value is closer to 1, suggesting the capacitive Li^+ storage behaviour is more dominant. On the contrary, the sluggish diffusion behaviour of batteries is more clear.

The CV curves of MoS_2/CP at various scan rates (Fig. 3c) display similar shapes even at 10 mV s^{-1}. It predicts superior rate performances. As for MoS_2/C, it presents roughly the same characteristics shown in Fig. S7b.† In contrast, the CV curves of bulk MoS_2 (Fig. S8b†) present obvious shape change and is not able to find its whole anodic peak while the scan rates increase to 10 mV s^{-1}. The phenomenon is attributed to the introduction of the conductive carbon matrix and the sufficient exfoliation of bulk MoS_2, which promote the rapid transfer of electrons and ions even in the face of biggish voltage/current changes.

The cathodic peak at 1.8 V and the anodic peak at 2.3 V are chosen to evaluate the b value. The results are shown in Fig. S9.† The b values of bulk MoS_2 are 0.49 and 0.50, which belongs to clear battery behaviour. The b values of MoS_2/C and MoS_2/CP

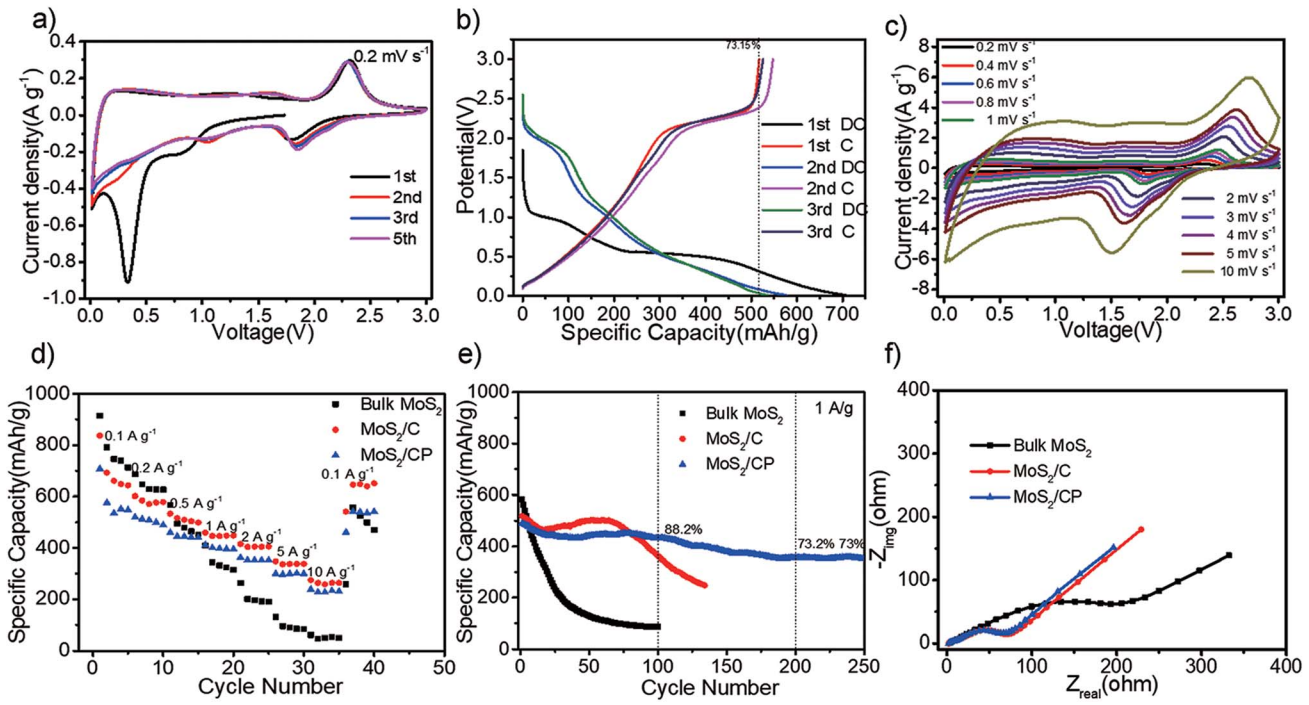

Fig. 3 Electrochemical property of half cells in the voltage window of 0.01–3.0 V. (a) CV graph of the MoS_2/CP at a scan rate of 1 mV s^{-1} for the first five laps, (b) GCD curves of MoS_2/CP at the current density of 0.1 A g^{-1} for 1st, 2nd and 3rd cycles. (c) CV curves of the MoS_2/CP at different scan rates. The rate performance (d), cycling stability (e) and EIS (f) of bulk MoS_2, MoS_2/C and MoS_2/CP.

are between 0.8 and 0.9, suggesting that they possess quicker response to the current changes compared with bulk MoS_2. The difference depends on the structural changes. After the ball-milling of MoS_2 and pyrolysis of carbon source, the ultrathin MoS_2 nanosheets with 3–7 layers are closely anchored on the carbon matrix through the Mo–O bond. The Li ion diffusion path is drastically reduced and more active sites in the plane and edge are exposed to Li^+ in the electrolyte. Thus the surface-controlled capacitive behavior is more obvious. While the bulk MoS_2 powder presents mostly battery behavior due to the integrated crystal structure. The conductive carbon matrix can accelerate the electron transport and prevent the delaminated MoS_2 nanosheets from aggregating together so that the *b* value of MoS_2/C and MoS_2/CP in the kinetics analysis is closer to 1.0. The performance improvement is achieved by the synergy between the MoS_2 and carbon.

When the three samples are tested by the galvanostatic charge/discharge measurement (GCD) with gradually increased current densities, MoS_2/C and MoS_2/CP both present superior rate performance than bulk MoS_2 and their capacity retention is about 43% even at the 100-times of initial current density as can be seen from Fig. 3d. These results imply that few-layered MoS_2 coated on the carbon matrix with high nitrogen content has short ion diffusion path, high electron conductivity and good interfacial wettability.[52] The consistent result can be obtained from the EIS data (Fig. 3f) where MoS_2/C and MoS_2/CP show smaller semicircles than bulk MoS_2 in the high frequency zone resulted from low charge transfer resistance (R_{ct}).[39,53] It should be pointed out that MoS_2/C shows higher capacity from above data because it has higher content of nitrogen (Table S1†) and MoS_2 mass ratio (Fig. 1f) than those of MoS_2/CP.[4,54] The role of carbon derived from pitch is to restrain the volume expansion for better cycling property.[35] We can see from Fig. 4e that the capacity of two samples increased gradually due to the activation,[55] and MoS_2/CP delivered superior cycle stability than MoS_2/C with the addition of pitch. The capacity retention of MoS_2/CP is 88.2% and 73% after 100 and 250 cycles at 1 A g^{-1}, respectively. The above results exhibit MoS_2/CP have potential advantages in LICs due to its high capacity, superior rate and cycle performance and rapid reaction kinetics.

As shown in Fig. 4a, the commercial AC (21 KS), which delivers superior rate property in the voltage windows of 1.5–4.5 V due to its great SSA (Fig. S10a†) and energy storage mode of physical adsorption, has been considered as a terrific capacitive electrode for LICs. The GCD curves of 21 KS (Fig. S11a†) present ideal linear and the capacity retention (Fig. S11b†) can maintain at 80% after 500 cycles. Therefore, the LICs are assembled by 21 KS and as-prepared MoS_2/CP in the organic electrolyte and the configuration of device is shown in Fig. S12a.† According to the potential distribution curves of the electrodes shown in Fig. S12b,† the voltage window of devices is optimized by using the pre-lithiated anode and finally set as 1.0–4.0 V conservatively to prevent Li metal from precipitating on the anode. The mass ratio of 21 KS to MoS_2/CP is adjusted in detail between 1.5 : 1 and 2.5 : 1 for the charge balance of cathode to anode ($Q_{cathode} = Q_{anode}$) and the optimum of energy and power property (Fig. 4b). Therefore, the optimum ratio 1.5 : 1 among them is determined in this device and the following tests are operated under the condition.

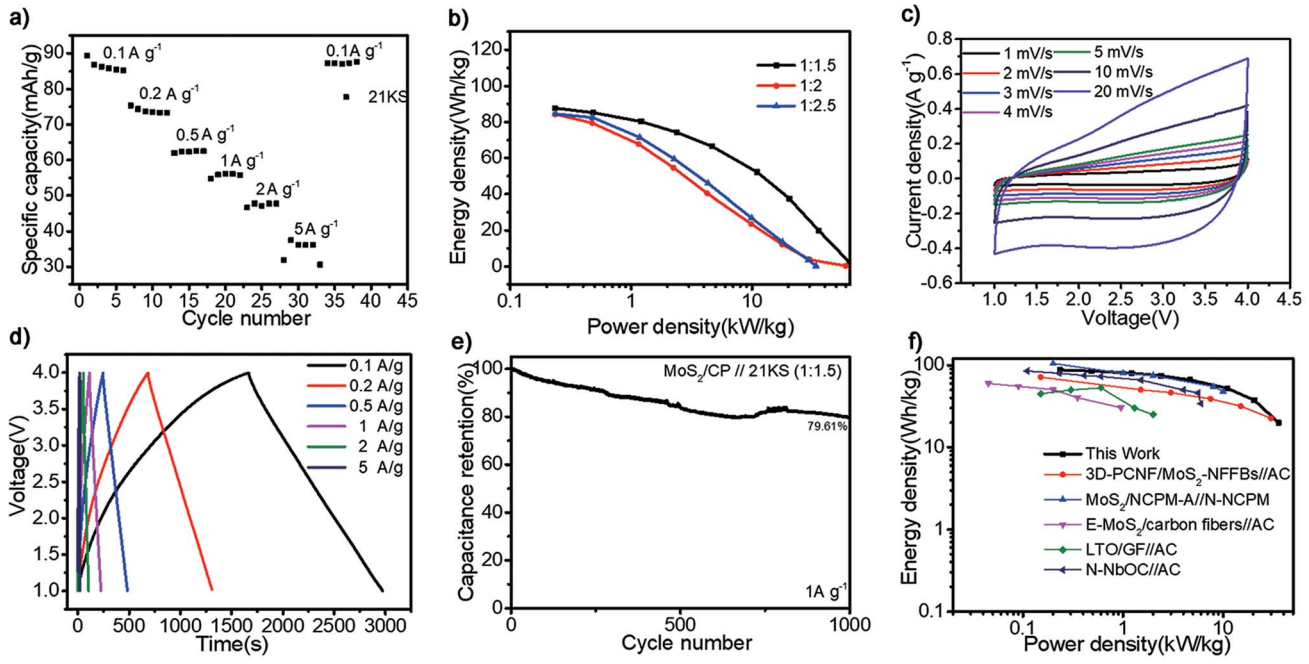

Fig. 4 MoS_2/CP//21 KS Li-ion capacitors (LICs) performance. (a) Rate performance of 21 KS, (b) Ragone plots of LICs at various mass ratios, (c) CV curves, (d) GCD profiles and (e) cycle stability of LICs at the mass ratio of 1.5 : 1. (f) Ragone plots of LICs compared with other latest reports (based on the total electrode mass).

The CV curves at increased scan rates (from 1 mV s^{-1} to 20 mV s^{-1}) are shown in Fig. 4c. At all scan rates, it exhibits regular rectangle without obvious redox peaks, indicative the typical capacitive behaviour and well-matching kinetics of the two electrodes.[6,56] The GCD profiles (Fig. 4d) present a standard triangle at various current densities with negligible IR drops, which is ascribed to the convenient ion diffusion and rapid charge transfer profited from N-doped carbon matrix and the adequate exfoliation of MoS_2.[45,57,58] The cycle stability (79.61% of initial capacity after 1000 cycles at 1 A g^{-1}) is shown in Fig. 4e. The power/energy property of device is shown in the Ragone plots (Fig. 4f). The LICs deliver the maximum energy density of 87.74 W h kg^{-1} at 253 W kg^{-1} and high power density of 35.81 kW kg^{-1} even at 19.86 W h kg^{-1}, which precedes other similar LICs systems reported recently, especially in the zone of high power density.[59–63]

Conclusions

In summary, we successfully synthesized the exfoliated MoS_2 supported by N-doped carbon matrix derived from chitosan, which is encapsulated by pitch-derived carbon shells by a simple ball-milling and pyrolysis method. It delivers high rate capability (530 mA h g^{-1} at 0.1 A g^{-1} and 230 mA h g^{-1} at 10 A g^{-1}) and cycle performance(73% capacity retention after 250 cycles) as the anode for LIBs, mainly ascribed to the sufficient exfoliation of MoS_2, conductive carbon matrix with high nitrogen content and robust carbon shells. Notably, the close contact between MoS_2 and carbon matrix through Mo–O bonds also have significant effect on the electrons and ions transfer. The LICs assembled by commercial AC (21 KS) as the cathode and MoS_2/CP as the anode present high energy density (87.74 W h kg^{-1}) and high power density (35.81 kW kg^{-1}) mainly profited from the fast Li^+ storage kinetics of the anode. The work provides an idea for constructing the devices with high energy and power densities by versatile and scalable methods.

Conflicts of interest

There are no conflicts to declare.

Acknowledgements

This work was supported by the National Natural Science Foundation of China (grant No. 51672151).

References

1 D. G. Nocera, *Chem. Soc. Rev.*, 2009, **38**, 13–15.
2 Z. Zhang, S. C. Mu, B. W. Zhang, L. Tao, S. F. Huang, Y. Z. Huang, F. M. Gao and Y. F. Zhao, *J. Mater. Chem. A*, 2016, **4**, 2137–2146.
3 Y. Gogotsi and P. Simon, *Science*, 2011, **334**, 917–918.
4 X. W. Dou, I. Hasa, D. Saurel, C. Vaalma, L. M. Wu, D. Buchholz, D. Bresser, S. Komaba and S. Passerini, *Mater. Today*, 2019, **23**, 87–104.
5 L. Ji, M. Gu, Y. Shao, X. Li, M. H. Engelhard, B. W. Arey, W. Wang, Z. Nie, J. Xiao, C. Wang, J. G. Zhang and J. Liu, *Adv. Mater.*, 2014, **26**, 2901–2908.
6 P. Simon, Y. Gogotsi and B. Dunn, *Science*, 2014, **343**, 1210–1211.
7 X. Li and L. Zhi, *Chem. Soc. Rev.*, 2018, **47**, 3189–3216.
8 S. Lee, G. Kwon, K. Ku, K. Yoon, S. K. Jung, H. D. Lim and K. Kang, *Adv. Mater.*, 2018, **30**, e1704682.
9 J. Ding, W. Hu, E. Paek and D. Mitlin, *Chem. Rev.*, 2018, **118**, 6457–6498.
10 J. Zhao, G. Wang, R. Hu, K. Zhu, K. Cheng, K. Ye, D. Cao and Z. Fan, *J. Mater. Chem. A*, 2019, **7**, 4047–4054.
11 X. Shen, J. He, K. Wang, X. Li, X. Wang, Z. Yang, N. Wang, Y. Zhang and C. Huang, *ChemSusChem*, 2019, **12**, 1342–1348.
12 P. Han, G. Xu, X. Han, J. Zhao, X. Zhou and G. Cui, *Adv. Energy Mater.*, 2018, **8**, 1801243.
13 S. Zheng, Z.-S. Wu, S. Wang, H. Xiao, F. Zhou, C. Sun, X. Bao and H.-M. Cheng, *Energy Storage Materials*, 2017, **6**, 70–97.
14 F. Yu, T. Huang, P. Zhang, Y. Tao, F.-Z. Cui, Q. Xie, S. Yao and F. Wang, *Energy Storage Materials*, 2019, **22**, 235–255.
15 A. Bhowmik, I. E. Castelli, J. M. Garcia-Lastra, P. B. Jørgensen, O. Winther and T. Vegge, *Energy Storage Materials*, 2019, **21**, 446–456.
16 C. Choi, D. S. Ashby, D. M. Butts, R. H. DeBlock, Q. Wei, J. Lau and B. Dunn, *Nat. Rev. Mater.*, 2019, DOI: 10.1038/s41578-019-0142-z.
17 G. G. Amatucci, F. Badway, A. Du Pasquier and T. Zheng, *J. Electrochem. Soc.*, 2001, **148**, A930–A939.
18 H. Wang, C. Zhu, D. Chao, Q. Yan and H. J. Fan, *Adv. Mater.*, 2017, **29**, 1702093.
19 D. P. Dubal, K. Jayaramulu, J. Sunil, Š. Kment, P. Gomez-Romero, C. Narayana, R. Zbořil and R. A. Fischer, *Adv. Funct. Mater.*, 2019, **29**, 1900532.
20 S. Li, H. Tang, P. Ge, F. Jiang, J. Zhou, C. Zhang, H. Hou, W. Sun and X. Ji, *ACS Appl. Mater. Interfaces*, 2018, **10**, 6378–6389.
21 P. Wang, J. Tian, J. Hu, X. Zhou and C. Li, *ACS Nano*, 2017, **11**, 7390–7400.
22 C. Z. Zhan, W. Liu, M. X. Hu, Q. H. Liang, X. L. Yu, Y. Shen, R. T. Lv, F. Y. Kang and Z. H. Huang, *NPG Asia Mater.*, 2018, **10**, 775–787.
23 T. Stephenson, Z. Li, B. Olsen and D. Mitlin, *Energy Environ. Sci.*, 2014, **7**, 209–231.
24 X. Zhou, L. J. Wan and Y. G. Guo, *Chem. Commun.*, 2013, **49**, 1838–1840.
25 L. Ma, B. Zhao, X. Wang, J. Yang, X. Zhang, Y. Zhou and J. Chen, *ACS Appl. Mater. Interfaces*, 2018, **10**, 22067–22073.
26 Y. Teng, H. Zhao, Z. Zhang, Z. Li, Q. Xia, Y. Zhang, L. Zhao, X. Du, Z. Du, P. Lv and K. Swierczek, *ACS Nano*, 2016, **10**, 8526–8535.
27 S. S. Xia, Y. R. Wang, Y. Liu, C. H. Wu, M. H. Wu and H. J. Zhang, *Chem. Eng. J.*, 2018, **332**, 431–439.
28 S. M. Cao, L. Y. Shi, M. Miao, J. H. Fang, H. B. Zhao and X. Feng, *Electrochim. Acta*, 2019, **298**, 22–30.
29 Y. G. Huang, Y. Wang, X. H. Zhang, F. Y. Lai, Y. N. Sun, Q. Y. Li and H. Q. Wang, *Mater. Lett.*, 2019, **243**, 84–87.

30 H. L. Xue, S. Yue, J. Wang, Y. Zhao, Q. Li, M. M. Yin, S. S. Wang, C. H. Feng, Q. Wu, H. S. Li, D. X. Shi and Q. Z. Jiao, *J. Electroanal. Chem.*, 2019, **840**, 230–236.
31 X. Wang, S. M. Fei, S. S. Huang, C. H. Wu, J. R. Zhao, Z. W. Chen, K. Uvdal and Z. J. Hu, *Carbon*, 2019, **150**, 363–370.
32 N. Feng, R. Meng, L. Zu, Y. Feng, C. Peng, J. Huang, G. Liu, B. Chen and J. Yang, *Nat. Commun.*, 2019, **10**, 1372.
33 D. Sun, D. L. Ye, P. Liu, Y. G. Tang, J. Guo, L. Z. Wang and H. Y. Wang, *Adv. Energy Mater.*, 2018, **8**, 11.
34 S. Chen, R. Xu, J. Liu, X. Zou, L. Qiu, F. Kang, B. Liu and H. M. Cheng, *Adv. Mater.*, 2019, **31**, e1804810.
35 G. Li, J. Y. Li, F. S. Yue, Q. Xu, T. T. Zuo, Y. X. Yin and Y. G. Guo, *Nano Energy*, 2019, **60**, 485–492.
36 F. Xie, Z. Xu, A. C. S. Jensen, H. Au, Y. Lu, V. Araullo-Peters, A. J. Drew, Y. S. Hu and M. M. Titirici, *Adv. Funct. Mater.*, 2019, **29**, 1901072.
37 Y. C. Jiao, A. Mukhopadhyay, Y. Ma, L. Yang, A. M. Hafez and H. L. Zhu, *Adv. Energy Mater.*, 2018, **8**, 1702779.
38 S. Wang, R. Wang, Q. Zhao, L. Ren, J. Wen, J. Chang, X. Fang, N. Hu and C. Xu, *J. Colloid Interface Sci.*, 2019, **544**, 37–45.
39 L. Q. Xu, Z. Jiao, P. F. Hu, Y. Wang, Y. J. Wang and H. J. Zhang, *Chemelectrochem*, 2016, **3**, 1503–1512.
40 M. R. Gao, M. K. Chan and Y. Sun, *Nat. Commun.*, 2015, **6**, 7493.
41 A. C. Ferrari, J. C. Meyer, V. Scardaci, C. Casiraghi, M. Lazzeri, F. Mauri, S. Piscanec, D. Jiang, K. S. Novoselov, S. Roth and A. K. Geim, *Phys. Rev. Lett.*, 2006, **97**, 187401.
42 J. Liu, Y. Zhang, L. Zhang, F. Xie, A. Vasileff and S. Z. Qiao, *Adv. Mater.*, 2019, **31**, e1901261.
43 W. Zhang, Y. Fu, W. Liu, L. Lim, X. Wang and A. Yu, *Nano Energy*, 2019, **57**, 48–56.
44 D. Xie, X. Xia, Y. Wang, D. Wang, Y. Zhong, W. Tang, X. Wang and J. Tu, *Chemistry*, 2016, **22**, 11617–11623.
45 J. X. Wu, Z. Y. Pan, Y. Zhang, B. J. Wang and H. S. Peng, *J. Mater. Chem. A*, 2018, **6**, 12932–12944.
46 R. Tian, W. Wang, Y. Huang, H. Duan, Y. Guo, H. Kang, H. Li and H. Liu, *J. Mater. Chem. A*, 2016, **4**, 13148–13154.
47 Z. Lei, L. Xu, Y. Jiao, A. Du, Y. Zhang and H. Zhang, *Small*, 2018, **14**, e1704410.
48 G. Huang, T. Chen, W. Chen, Z. Wang, K. Chang, L. Ma, F. Huang, D. Chen and J. Y. Lee, *Small*, 2013, **9**, 3693–3703.
49 X. P. Fang, X. Q. Yu, S. F. Liao, Y. F. Shi, Y. S. Hu, Z. X. Wang, G. D. Stucky and L. Q. Chen, *Microporous Mesoporous Mater.*, 2012, **151**, 418–423.
50 V. Augustyn, J. Come, M. A. Lowe, J. W. Kim, P. L. Taberna, S. H. Tolbert, H. D. Abruna, P. Simon and B. Dunn, *Nat. Mater.*, 2013, **12**, 518–522.
51 H.-S. Kim, J. B. Cook, H. Lin, J. S. Ko, S. H. Tolbert, V. Ozolins and B. Dunn, *Nat. Mater.*, 2016, **16**, 454–460.
52 M. Wang, Z. Yang, W. Li, L. Gu and Y. Yu, *Small*, 2016, **12**, 2559–2566.
53 G. A. Elia, U. Ulissi, S. Jeong, S. Passerini and J. Hassoun, *Energy Environ. Sci.*, 2016, **9**, 3210–3220.
54 J. Y. Jin, Z. W. Wang, R. Wang, J. L. Wang, Z. D. Huang, Y. W. Ma, H. Li, S. H. Wei, X. Huang, J. X. Yan, S. Z. Li and W. Huang, *Adv. Funct. Mater.*, 2019, **29**, 1807441.
55 Y. Y. Liu, L. Zhang, Y. C. Zhao, T. D. Shen, X. L. Yan, C. Yu, H. Q. Wang and H. Zeng, *J. Alloys Compd.*, 2019, **787**, 996–1003.
56 Y. Gogotsi and R. M. Penner, *ACS Nano*, 2018, **12**, 2081–2083.
57 D. Ni, W. Sun, Z. Wang, Y. Bai, H. Lei, X. Lai and K. Sun, *Adv. Energy Mater.*, 2019, **9**, 1900036.
58 D. F. Xu, C. J. Chen, J. Xie, B. Zhang, L. Miao, J. Cai, Y. H. Huang and L. N. Zhang, *Adv. Energy Mater.*, 2016, **6**, 1501929.
59 S. Hemmati, G. Li, X. L. Wang, Y. L. Ding, Y. Pei, A. P. Yu and Z. W. Chen, *Nano Energy*, 2019, **56**, 118–126.
60 J. Jiang, Y. Zhang, Y. An, L. Wu, Q. Zhu, H. Dou and X. Zhang, *Small Methods*, 2019, 1900081.
61 C. T. Zhao, C. Yu, M. D. Zhang, Q. Sun, S. F. Li, M. N. Banis, X. T. Han, Q. Dong, J. Yang, G. Wang, X. L. Sun and J. S. Qiu, *Nano Energy*, 2017, **41**, 66–74.
62 Y. Qian, X. Y. Cai, C. Y. Zhang, H. F. Jiang, L. J. Zhou, B. S. Li and L. F. Lai, *Electrochim. Acta*, 2017, **258**, 1311–1319.
63 J. G. Ju, L. T. Zhang, H. S. Shi, Z. J. Li, W. M. Kang and B. W. Cheng, *Appl. Surf. Sci.*, 2019, **484**, 392–402.